Modeling and Analysis of a Digitally Controlled Grid-Connected Large-Scale Centralized PV System

Jinhong Liu, Lin Zhou, Bin Li, Chen Zheng, and Bao Xie

***Abstract*—Multi-inverter systems have been widely used for grid-connected large-scale centralized photovoltaic (LSCPV) plants. However, the problem of how time delays affect the stability of digitally controlled grid-connected LSCPV plants with multi-inverter systems has not been investigated sufficiently. This paper models a grid-connected LSCPV system as a cascade system and conducts a systematic study of the relationship between the time delay and the stability of a grid-connected LSCPV system. The analysis intuitively reveals the influence of the time delay on the stability of the grid-connected LSCPV system. The impact of the time delay on the stability range of the number of grid-connected inverters in LSCPV plants is discussed for the first time, and the stability range for a specific time delay is obtained from the root locus. In addition, considering the damping performance is negatively affected by the time delay, an improved capacitor-current-feedback active damping method is proposed to reduce the effects of the delay on the damping region and the robustness against variations in the grid impedance. Simulations and experimental results are presented to validate the theoretical analysis and the effectiveness of the proposed delay compensation method.**

***Index Terms*—Allowable inverter number, delay compensation, digitally controlled, large-scale centralized photovoltaic (LSCPV) plants, time delay.**

I. Introduction

THE photovoltaic industry has developed rapidly in recent years. According to the latest market data from Solarbuzz, the total installed capacity of the global photovoltaic (PV) power generation system was approximately 294 GW in 2016. In addition to having a higher power output than small-scale PV (SSPV) plants, large-scale centralized PV (LSCPV) plants have more significant opportunities for using parallel inverter technologies with centralized management and control as a strategy to promote the efficient utilization of solar energy. Under appropriate conditions, LSCPV plants can provide grid-friendly functionality, such as peak-clipping and reactive compensation, by employing solar distribution characteristics and energy storage technology. Therefore, LSCPV plants have become an important development trend in PV and have drawn increasing amounts of attention with the steady decrease in the cost of LSCPV plants and the continual increase in generation benefits [1]–[4].

Although LSCPV plants have been widely implemented due to their high efficiency and multifunctionality, they still exhibit several problems during grid connection. Because LSCPV plant sites are typically located far from load centers, a transmission network, which primarily consists of a stepup transformer and transmission lines, is needed to convey electricity from LSCPV plants to distant load centers. However, with the use of the transmission network, an impedance will be introduced to the multi-inverter system of a grid-connected LSCPV plant through the point of common coupling (PCC); this allows the current of the grid-connected inverter to circulate between the inverters and between the inverter and the power grid, which influences the quality of the power supply and the stability of the grid-connected system. Furthermore, the interaction between PV plants and the power grid will become increasingly significant with increases in PV plant capacity [4]–[10].

To address these problems, many studies have been devoted to the modeling, analysis, and control of grid-connected systems [4]–[20]. Li *et al.* [5] investigated a full-feedforward scheme of grid voltages based on a model of a grid-connected inverter with an LCL filter and proposed a full-feedforward function of the grid voltages to reduce the grid current distortion of the grid-connected inverter. Since the obtained model of grid-connected inverters is relatively complex and inconvenient to use in the analysis of grid-connected systems, Sun [6] proposed an impedance-based stability criterion to analyze the stability of a single grid-connected inverter system based on the inverter output impedance and grid impedance, and [4], [7], and [8] built a Norton equivalent circuit of a grid-connected multi-inverter system and investigated stability issues of inverters that operate in parallel. Lazzarin *et al.* [9] employed two control loops to avoid current circulation between the inverters and to ensure the proper sharing of the load current, and He and Li [10] proposed a generalized closed-loop control scheme with embedded internal and external virtual impedance terms to improve the system stability and damping relative to that of conventional controllers. However, time delays were not considered in the modeling and analysis of grid-connected inverter systems in these studies; thus, these analyses and methods may be inappropriate or insufficient for a digitally controlled grid-connected system.

Manuscript received April 9, 2017; accepted May 30, 2017. Date of publication June 7, 2017; date of current version February 1, 2018. This work was supported in part by the National Nature Science Foundations of China under Grant 51477021 and in part by the National "111" Project of China under Grant B08036. Recommended for publication by Associate Editor D. Xu. *(Corresponding author: Jinhong Liu.)*

The authors are with the of Electrical Engineering, Chongqing University, Chongqing 400044, China (e-mail: jinhongliu_felix@163.com; zhoulin@cqu.edu.cn; 20956623@qq.com; 1837187510@qq.com; 1261889141@qq.com).

Color versions of one or more of the figures in this paper are available online at http://ieeexplore.ieee.org.

Digital Object Identifier 10.1109/TPEL.2017.2712910

With the increasing performance-price ratio of digital signal processors (DSPs), fully digital control has been widely used to replace analog control in high-power switching converters [11]. However, the use of digital control introduces a time delay into the control system, which will influence the system stability [11]–[17]. Therefore, to analyze digitally controlled systems more accurately, researchers have begun to integrate the time delay into the modeling of grid-connected inverters [11]–[17]. Since the time delay changes with variations in the duty ratio update mode, a small signal method was proposed to model grid-connected inverters with different time delays under the most common circumstances [11]. Based on the obtained model, Wang *et al.* [12] investigated the stability of single-loop grid-connected inverters and obtained a stable range of the time delay. A linear predictor was also adopted to realize the time delay compensation in [12]. Miskovic *et al.* [13] adopted a Luenberger observer to perform the time delay compensation, but the state observer is sensitive to changes of the system parameters, and the observer may be invalid when the situation changes. In addition to the direct-delay-compensation methods discussed above, many publications have also explored methods to enhance the stability of the system by extending the damping region, which is decreased by the time delay [14]–[18]. One-sixth of the sampling frequency ($f_s/6$) was proven to be the critical frequency for the stability of a digitally controlled LCL-type grid-connected inverter [14]–[18]. Therefore, a system damping region compensation method was proposed in [14] and [15] to increase the critical frequency, which is directly related to the damping region, from $f_s/6$ to approximately $0.25\,f_s$. However, since the systems in previous papers were discussed for the case of a switching frequency equal to half of the sampling frequency, the critical frequency may not be sufficiently high to ensure stability if the ratio of the switching frequency to the sampling frequency is changed. In addition to studies on the stability of single grid-connected inverters with a time delay, parallel multi-inverter systems with a time delay have also been discussed in several publications due to the large number of applications for this type of system [19]–[21]. Turner *et al.* [19] demonstrated the bandwidth limitations that occur in grid-connected parallel multi-inverter systems when considering the time delay. Zhang and Ma [20] presented methodologies for predicting the stability of a parallel multi-inverter system with networked control while considering the time delay. He *et al.* [21] developed a model of a microgrid with *N* parallel inverters in the z-domain with consideration of the time delay and investigated the resonance problem in the microgrid system using the model.

The influences of the time delay, control strategy, grid impedance, and other system factors on single grid-connected inverter systems were researched in depth in the papers discussed above [11]–[18]. However, studies on digitally controlled multi-inverter grid-connected systems have primarily concentrated on the effects of the grid impedance on the stability of the system [4], [19]–[21], and few studies have focused on the effects of time delays on grid-connected multi-inverter systems, even when the time delay is considered in the modeling of multi-inverter systems.

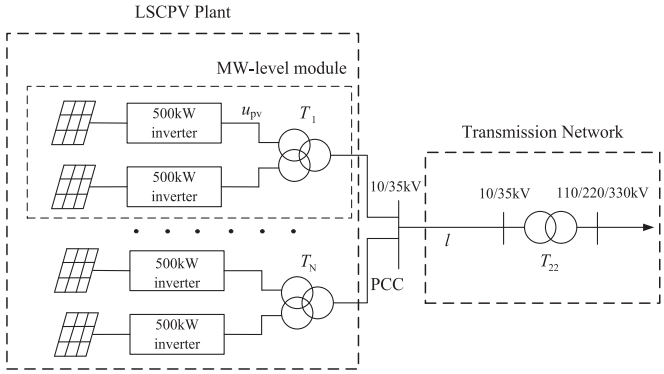

Fig. 1. Main topology of the grid-connected LSCPV system.

Therefore, this paper focuses on building a model of a digitally controlled grid-connected LSCPV system and analyzing the effects of the time delay on the system stability. A method for extending the damping region is proposed to improve the stability and robustness of the system. In Section II, the digitally controlled grid-connected LSCPV system is modeled in detail. Then, based on the obtained grid-connected LSCPV system model, an impedance-based criterion is used to clearly identify the effects of the time delay on the stability of grid-connected LSCPV systems in Section III. The effects of the time delay on the stability range of the number of grid-connected inverters in LSCPV plants is discussed using the root locus, and an improved capacitor-current feedback is proposed to improve the system damping performance by extending the damping region. The theoretical analysis is verified by simulations and experimental results in Section IV, and Section V concludes the paper.

II. Modeling of the Grid-Connected LSCPV System

A. System Description

The main topology of the grid-connected LSCPV system, which mainly consists of an LSCPV plant, split-winding transformers T_N, a medium-/low-voltage transmission line*l*and a large-capacity stepup transformer T_{22}, is shown in Fig. 1. The circuit of the grid-connected inverters in the LSCPV plant is shown in Fig. 2(a), where the dc bus of the inverter is considered an ideal constant dc voltage source $V_{\rm dc}$, and the parasitic resistance associated with the inductor is neglected. The equivalent single-phase circuit is shown in Fig. 2(b), where u_i is the inverter output voltage, and $u_{\rm pv}$ is the output voltage of the inverter.

The control strategy that is typically used in grid-connected inverters in PV plants is a cascaded-loop control [3], [4], [7]. The outer loop controls the voltage of the dc bus and can be ignored in the analysis of the system when the dc bus is considered to be an ideal constant dc voltage source, as shown in Fig. 2(a). To complete the control of the grid-side current i_s, the grid-side current i_s and capacitor current i_c are sensed as the feedback variables for the inner loop of the inverter control system, where the capacitor current i_c is measured to implement the active damping in the LCL circuit. Since the grid-side current reference

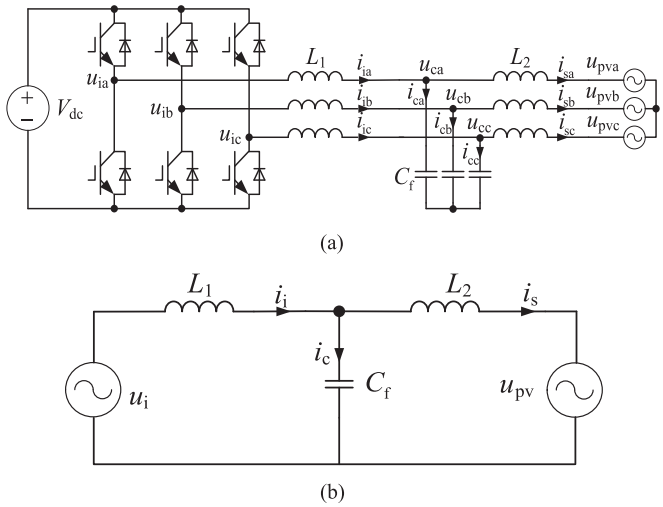

Fig. 2. Grid-connected inverter with an LCL filter in an LSCPV plant. (a) Power circuit. (b) Equivalent single-phase circuit.

i_s^* is used to control the system stability, the output voltage of the inverter behaves as a disturbance and can be considered to be equal to zero when describing the modeling and stability of the grid-connected inverters.

B. Modeling of the Transmission Network

Because the main power network, which includes the 220 kV and a higher extra-high-voltage long-distance transmission network and its power network, can be considered to be equivalent to an ideal voltage source, the modeling of the transmission network in this section primarily focuses on the large-capacity stepup transformer and the medium- and low-voltage transmission lines, which are between the LSCPV plant and the main power network.

In the power system calculation, the reactance of a large-capacity transformer is approximately equal to the modulus of its impedance [22], [23]. Thus, because the resistance can be neglected, the percent impedance $U_k(\%)$ of a transformer can be expressed as

$$U_k(\%) = \frac{\sqrt{3} I_N Z_T}{U_N} \times 100 \approx \frac{\sqrt{3} I_N X_T}{U_N} \times 100 \tag{1}$$

where U_N and I_N represent the rated voltage and rated current of the transformer, respectively, Z_T and X_T are the impedance and reactance of the transformer, respectively.

Therefore, the large-capacity transformers can be considered to be equivalent to an inductance, which can be derived from (1) as

$$L_{TT} = \frac{U_k(\%) U_N^2}{100 \omega_0 S_N} \tag{2}$$

where S_N is the rated capacity of the transformer and ω_0 is the fundamental angular frequency of the grid.

Since the transmission lines of 35 kV or less are typically used to convey electricity from the LSCPV plant to large-capacity stepup transformers, the transmission line in the grid-connected

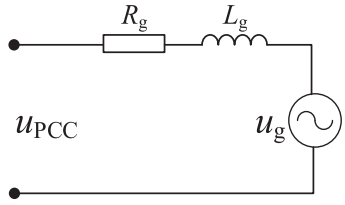

Fig. 3. Equivalent circuit model of the transmission network.

LSCPV system can be represented as an impedance and is expressed as

$$Z_l = rl + jxl \tag{3}$$

where *l* is the length of the transmission line, and *r* and *x* are the resistance and reactance of the transmission line per unit length, respectively.

From (2) and (3), the expression of the equivalent impedance of the transmission network in the *s*-domain can be derived as

$$Z_{\rm tr}(s) = L_{\rm tr} s + R_{\rm tr} = \left(L_{TT} + \frac{xl}{\omega_0} \right) s + rl \tag{4}$$

where $L_{\rm tr}$ is the equivalent inductance of the transmission network, and $R_{\rm tr}$ is the equivalent resistance of the transmission network. To facilitate the modeling and analysis, the equivalent impedance of the transmission network from (4) can be related to the low-voltage side of the split-winding transformer by

$$Z_g(s) = L_g s + R_g = k^2 Z_{\rm tr}(s) = k^2 \left(L_{TT} + \frac{xl}{\omega_0} \right) s + k^2 rl \tag{5}$$

where *k* is the turns ratio of the split-winding transformer, and L_g and R_g are the inductance and resistance, respectively, of the transmission network with respect to the low-voltage side of the split-winding transformer. The equivalent model of the transmission network in the grid-connected LSCPV system is shown in Fig. 3, where u_g and $u_{\rm PCC}$ represent the grid-side voltage and PCC voltage referenced to the low-voltage side of the split-winding transformer, respectively.

C. Modeling of the LSCPV Plant

To implement an independent control in the control loop without using a decoupling module, the scheme of the inner control loop for the grid-side current i_s is developed in a stationary frame, as shown in Fig. 4, where $G_c(s)$ is the current controller, and a proportional-resonant (PR) controller is used

$$G_c(s) = k_p + \frac{2 k_r \omega_i s}{s^2 + 2\omega_i s + \omega_0^2}. \tag{6}$$

The synchronous sampling method is adopted to obtain the average value of the current in a switching period and to avoid switching noise [12]. Using a digital control system, the computation process of the DSP microprocessor gives rise to a time delay of one sampling period (T_s) that can be given by [12] and [16]

$$G_d(s) = e^{-sT_s}. \tag{7}$$

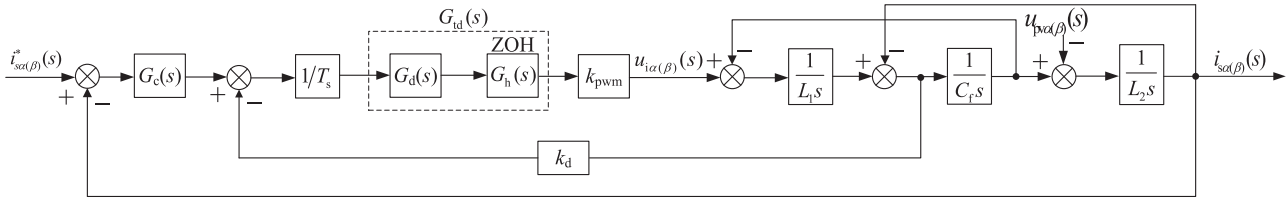

Fig. 4. Single inverter control loop for the grid-side current.

With the pulse-width-modulation (PWM) reference updated, it will be held on and compared to the triangular carrier to generate the duty cycle. This process can be modeled as a zero-order-hold, which results in a delay of $0.5T_s$ and can be expressed as [16], [25]

$$G_h(s) = \frac{1 - e^{-sT_s}}{s} \approx T_s e^{-0.5sT_s}. \tag{8}$$

After combining (7) and (8), the transfer function of the total delay in the control loop can be expressed as

$$G_{td}(s) = T_s e^{-1.5sT_s}. \tag{9}$$

Since an exponential expression is not convenient for the analysis of the system stability, (9) is commonly used by means of a second-order *Padé* approximation [24], [25], which is expressed by

$$G_{td}(s) \approx T_s \frac{(1.5sT_s)^2 - 9T_s s + 12}{(1.5sT_s)^2 + 9T_s s + 12}. \tag{10}$$

Furthermore, k_d is the active damping coefficient**,** which is used to achieve active damping of the resonance of the LCL circuit. The transfer function of the inverter is represented by $k_{\rm pwm}$, which is expressed as $k_{\rm pwm} = V_{\rm dc}/V_c$, where $V_{\rm dc}$ is the dc-side voltage, and $V_{\rm c}$ is the amplitude of the carrier.

From Fig. 4, the relationship between the grid-side current $i_{s\rm mn}$, the grid-side current reference $i^*_{s\rm mn}$, and the PCC voltage $u_{\rm PCC}$ in the *n*th inverter of the *m*th MW-level module can be obtained by (11), where $G_{s\rm mn}(s) = k_{\rm pwm}G_{td\rm mn}(s)$, $\omega_{r\rm mn} = \sqrt{1/(L_{2\rm mn}C_{f\rm mn})}$, $\omega_{\rm resmn} = \sqrt{(L_{1\rm mn}+L_{2\rm mn})/(L_{1\rm mn}L_{2\rm mn}C_{f\rm mn})}$, $n = 2m (0 < m \le N)$, and *N* represents the total number of split-winding transformers in the LSCPV plant

$$\begin{bmatrix} i_{s\rm mn\alpha}(s) \\ i_{s\rm mn\beta}(s) \end{bmatrix} = G_{\rm mn}(s) \begin{bmatrix} i^*_{s\rm mn\alpha}(s) \\ i^*_{s\rm mn\beta}(s) \end{bmatrix} - Y_{\rm eqmn}(s) \begin{bmatrix} u_{\rm pv\alpha}(s) \\ u_{\rm pv\beta}(s) \end{bmatrix} \tag{11}$$

where, see (12) and (13) shown at the bottom of this page.

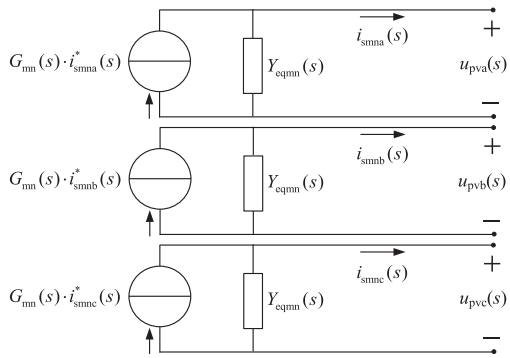

Fig. 5. Norton model of the three-phase inverter.

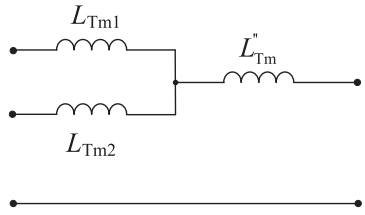

Fig. 6. Equivalent model of the split-winding transformer.

With an inverse Clarke transform, (11) can be transformed into three-phase static coordinates as

$$\begin{bmatrix} i_{s\rm mna}(s) \\ i_{s\rm mnb}(s) \\ i_{s\rm mnc}(s) \end{bmatrix} = G_{\rm mn}(s) \begin{bmatrix} i^*_{s\rm mna}(s) \\ i^*_{s\rm mnb}(s) \\ i^*_{s\rm mnc}(s) \end{bmatrix} - Y_{\rm eqmn}(s) \begin{bmatrix} u_{\rm pva}(s) \\ u_{\rm pvb}(s) \\ u_{\rm pvc}(s) \end{bmatrix}. \tag{14}$$

Fig. 5 shows the Norton model of a single three-phase inverter based on (14). Because the three-phase inverter model is interphase decoupled, an A-phase equivalent Norton model of the grid-connected LSCPV system is built and used to analyze the stability of the entire grid-connected LSCPV system in the following sections.

Based on the characteristics of split-winding transformers, which are widely used in LSCPV plants, the split-winding transformer T_N in Fig. 1 is presented in Fig. 6, and the leakage inductances of the high-voltage side (L''_{TN}) and the low-voltage

$$G_{\rm mn}(s) = \frac{G_{s\rm mn}(s)\omega^2_{r\rm mn}G_{c\rm mn}(s)}{L_{1\rm mn}s^3 + k_{d\rm mn}G_{s\rm mn}(s)s^2 + L_{1\rm mn}\omega^2_{\rm resmn}s + G_{s\rm mn}(s)G_{c\rm mn}(s)\omega^2_{r\rm mn}} \tag{12}$$

$$Y_{\rm eqmn}(s) = \frac{(L_{1\rm mn}/L_{2\rm mn})s^2 + (k_{d\rm mn}G_{s\rm mn}(s)/L_{2\rm mn})s + \omega^2_{r\rm mn}}{L_{1\rm mn}s^3 + k_{d\rm mn}G_{s\rm mn}(s)s^2 + L_{1\rm mn}\omega^2_{\rm resmn}s + G_{s\rm mn}(s)G_{c\rm mn}(s)\omega^2_{r\rm mn}} \tag{13}$$

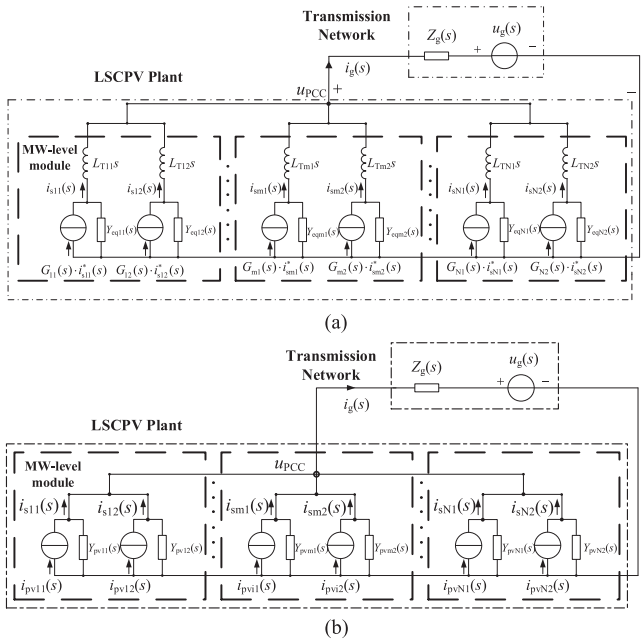

Fig. 7. A-phase model of the grid-connected LSCPV system. (a) A-phase equivalent model of the grid-connected LSCPV system. (b) Simplified A-phase equivalent model of the grid-connected LSCPV system.

side (L_{Tm1} and L_{Tm2}, respectively) satisfy $L_{Tm1} = L_{Tm2}$, $L''_{Tm} \approx 0$ [26].

Fig. 7(a) shows the Norton equivalent model of the A-phase grid-connected LSCPV system after combining the transmission network model with the LSCPV plant model, where L_{Tm1} and T_{Tm2} represent the leakage inductances of the low-voltage sides of the split-winding transformers.

When each inverter in the LSCPV plant is stable, the current reference $G_{\mathrm{mn}}(s) \cdot i^*_{s\mathrm{mn}}(s)$ and the admittance Y_{eqmn} in Fig. 7(a) are rearranged as shown in (15) and (16), respectively, and the equivalent model of the grid-connected LSCPV system in Fig. 7(a) can be further simplified to that depicted in Fig. 7(b)

$$i_{\mathrm{pvmn}}(s) = \frac{G_{\mathrm{mn}}(s) i^*_{\mathrm{smn}}(s)}{Y_{\mathrm{eqmn}}(s) L_{Tmn} s + 1} \tag{15}$$

$$Y_{\mathrm{pvmn}}(s) = \frac{Y_{\mathrm{eqmn}}(s)}{Y_{\mathrm{eqmn}}(s) L_{Tmn} s + 1}. \tag{16}$$

By applying a superposition method to Fig. 7(b), the grid-side current of the *n*th grid-connected inverter of the *m*th MW-level module in the grid-connected LSCPV system can be derived as

$$\begin{aligned} i_{s\mathrm{mn}}(s) = &\left(1 - \frac{Y_{\mathrm{pvmn}}(s)}{\sum_{m=1}^{N}\sum_{n=1}^{2} Y_{\mathrm{pvmn}}(s) + Y_g(s)}\right) i_{\mathrm{pvmn}} \\ &- \frac{Y_{\mathrm{pvmn}}(s) Y_g(s)}{\sum_{m=1}^{N}\sum_{n=1}^{2} Y_{\mathrm{pvmn}}(s) + Y_g(s)} u_g(s) \\ &- \sum_{t=1}^{N}\sum_{h=1,h\neq n}^{2} \frac{Y_{\mathrm{pvmn}}(s)}{\sum_{m=1}^{N}\sum_{n=1}^{2} Y_{\mathrm{pvmn}}(s) + Y_g(s)} i_{\mathrm{pvth}}(s). \end{aligned} \tag{17}$$

Equation (17) indicates that the inverters in the grid-connected LSCPV system are coupled and interact with one another, which reduces the output power quality and can even destabilize the grid-connected LSCPV system [4], [11]–[13].

III. Analysis of the Delay-Dependent Stability of Grid-Connected LSCPV System

Because the inverters that are installed in the majority of LSCPV plants are typically manufactured by the same company and are of the same type, the parameters of the grid-connected inverters in the LSCPV plant are assumed to be the same. Based on the model of the grid-connected LSCPV system that was obtained in Section II, the influence of the time delay on the grid-connected LSCPV system is discussed in this section.

A. Effects of the Time Delay on the Stability of Grid-Connected LSCPV System

Although the effects of a time delay on the stability of grid-connected multi-inverter systems have been discussed in several publications [11]–[13], it is necessary to discuss them again in the context of a digitally controlled grid-connected LSCPV system. A different method is employed to intuitively demonstrate the influence of the time delay on the stability of a grid-connected LSCPV system.

The simplified grid-connected LSCPV system model in Fig. 7(b) illustrates that the grid-connected LSCPV plant is equivalent to a current source (i_{pv}) in parallel with an output admittance (Y_{pv}) and in series with a grid impedance (Z_g) and a grid voltage (u_g). Therefore, the effects of the time delay on the stability of the grid-connected LSCPV system can be evaluated using the impedance-based stability criterion [6].

Because the parameters of the grid-connected inverters in the LSCPV plant are the same, (17) can be simplified as

$$\begin{aligned} i_{s\mathrm{mn}}(s) = &\left(1 - \frac{Y_{\mathrm{pv}}(s)}{2NY_{\mathrm{pv}}(s) + Y_g(s)}\right) i_{\mathrm{pvmn}} \\ &- \frac{Y_{\mathrm{pv}}(s) Y_g(s)}{2NY_{\mathrm{pv}}(s) + Y_g(s)} u_g(s) \\ &- \sum_{t=1}^{N}\sum_{h=1,h\neq n}^{2} \frac{Y_{\mathrm{pv}}(s)}{2NY_{\mathrm{pv}}(s) + Y_g(s)} i_{\mathrm{pvth}}(s). \end{aligned} \tag{18}$$

Then, (18) can be rearranged to

$$\begin{aligned} i_{s\mathrm{mn}}(s) = &\{[1 + 2NY_{\mathrm{pv}}(s)/Y_g(s) - Y_{\mathrm{pv}}(s)/Y_g(s)] i_{\mathrm{pvmn}} \\ &- Y_{\mathrm{pv}}(s) u_g(s) - \sum_{t=1}^{N}\sum_{h=1,h\neq n}^{2} [Y_{\mathrm{pv}}(s)/Y_g(s)] i_{\mathrm{pvth}}(s)\} \\ &\frac{1}{1 + 2NY_{\mathrm{pv}}(s)/Y_g(s)}. \end{aligned} \tag{19}$$

The following two assumptions are made based on the impedance-based criterion to analyze the stability of a grid-connected LSCPV system:

1) the LSCPV plant is stable when it is off the grid; i.e., (15) has no unstable poles;

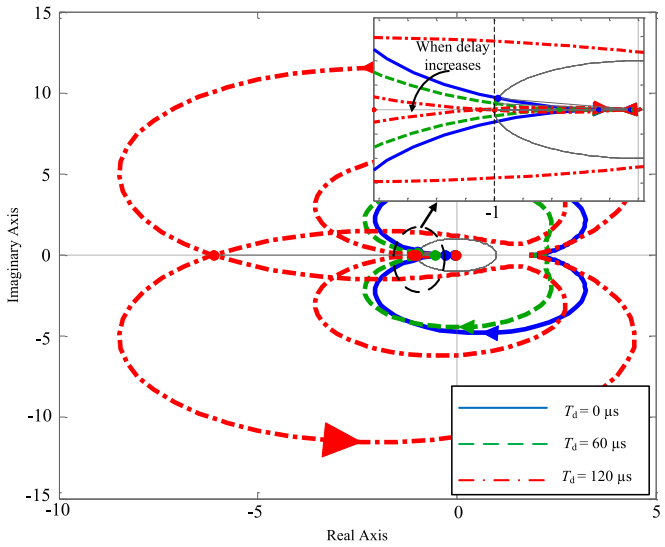

Fig. 8. Nyquist diagrams of $2NY_{\rm pv}(s)/Y_g(s)$ for time delays (T_d) of 0, 60 and 120 μs.

2) the grid is stable when it is connected to the LSCPV plants; i.e., the transmission network impedance Z_g has no right half-plane zeros.

In this case, $i_{\rm pvmn}$, $i_{\rm pvth}$, and u_g are stable, and the stability of the grid-side current i_{smn} depends on the stability of the second term on the right-hand side of (19)

$$H(s)=\frac{1}{1+2NY_{\rm pv}(s)/Y_g(s)}. \tag{20}$$

By linear control theory, $H(s)$ resembles a closed-loop transfer function of a negative feedback control system that has a unit forward gain, and the feedback gain is $2NY_{\rm pv}(s)/Y_g(s)$. Therefore, the stability of H(s) depends on whether $2NY_{\rm pv}(s)/Y_g(s)$ satisfies the Nyquist stability criterion. When the other system parameters are determined, the influence of the time delay on the stability of the grid-connected LSCPV system can be evaluated using the Nyquist diagram of $2NY_{\rm pv}(s)/Y_g(s)$, which is shown in Fig. 8. As the time delay increases, the Nyquist curves gradually approach (–1, *j*0), and the system stability margin is reduced. When the time delay increases to 120 μs, the point (–1, *j*0) is enclosed by the Nyquist curve, which indicates that a larger time delay leads to a lower system stability, and the system may become unstable when the time delay exceeds a certain value.

B. Effects of the Time Delay on the Stability Range of the Number of Grid-Connected Inverters

Because the number of grid-connected inverters (2*N*) is directly related to the grid-connected capacity of the LSCPV plants, the effects of the time delay on the stability range of the number of grid-connected inverters should also be considered to achieve stable operation of the grid-connected LSCPV system.

Substituting (15) into (18) leads to the closed-loop transfer function of the grid-side current, which is given by

$$\begin{aligned} i_{smn}(s)=&\left[1-\frac{Y_{\rm eq}(s)}{2NY_{\rm eq}(s)+Y_g(s)\left(Y_{\rm eq}(s)L_Ts+1\right)}\right]\\ &\cdot\frac{G(s)}{Y_{\rm eq}(s)L_Ts+1}i^*_{smn}(s)\\ &-\frac{Y_{\rm eq}(s)Y_g(s)}{2NY_{\rm eq}(s)+Y_g(s)\left(Y_{\rm eq}(s)L_Ts+1\right)}u_g(s)\\ &-\frac{Y_{\rm eq}(s)}{2NY_{\rm eq}(s)+Y_g(s)\left(Y_{\rm eq}(s)L_Ts+1\right)}\\ &\cdot\frac{G(s)}{Y_{\rm eq}(s)L_Ts+1}\sum_{t=1}^{N}\sum_{h=1,h\neq n}^{2}i^*_{\rm th}(s). \end{aligned} \tag{21}$$

From Fig. 7(b), the PCC voltage of the LSCPV plant can be derived as

$$\begin{aligned} u_{\rm PCC}(s)=&\frac{1}{2NY_{\rm pv}(s)+Y_g(s)}\sum_{t=1}^{N}\sum_{h=1}^{2}i_{\rm pvth}(s)\\ &+\frac{Y_g(s)}{2NY_{\rm pv}(s)+Y_g(s)}u_g(s). \end{aligned} \tag{22}$$

After substituting (15) into (22), the closed-loop transfer function of the PCC voltage can be obtained as

$$\begin{aligned} u_{\rm PCC}(s)=&\frac{Y_{\rm eq}(s)L_Ts+1}{2NY_{\rm eq}(s)+Y_g(s)\left(Y_{\rm eq}(s)L_Ts+1\right)}\\ &\cdot\frac{G(s)}{Y_{\rm eq}(s)L_Ts+1}\sum_{t=1}^{N}\sum_{h=1}^{2}i^*_{\rm th}(s)\\ &+\frac{Y_g(s)\left(Y_{\rm eq}(s)L_Ts+1\right)}{2NY_{\rm eq}(s)+Y_g(s)\left(Y_{\rm eq}(s)L_Ts+1\right)}u_g(s). \end{aligned} \tag{23}$$

If the grid-side voltage u_g and the current reference $i^*_{\rm th}$ of the other inverters are considered as disturbances, (21) and (23) can be further simplified as

$$\begin{aligned} i_{smn}(s)=&\left[1-\frac{Y_{\rm eq}(s)}{2NY_{\rm eq}(s)+Y_g(s)\left(Y_{\rm eq}(s)L_Ts+1\right)}\right]\\ &\cdot\frac{G(s)}{Y_{\rm eq}(s)L_Ts+1}i^*_{smn}(s) \end{aligned} \tag{24}$$

$$\begin{aligned} u_{\rm PCC}(s)=&\frac{Y_{\rm eq}(s)L_Ts+1}{2NY_{\rm eq}(s)+Y_g(s)\left(Y_{\rm eq}(s)L_Ts+1\right)}\\ &\cdot\frac{G(s)}{Y_{\rm eq}(s)L_Ts+1}\sum_{t=1}^{N}\sum_{h=1}^{2}i^*_{\rm th}(s). \end{aligned} \tag{25}$$

Note that the characteristic (24) and (25) are the same and can be expressed as

$$\begin{aligned} f(s)=&a_0+a_1s+a_2s^2+a_3s^3+a_4s^4+a_5s^5+a_6s^6\\ &+a_7s^7+a_8s^8+a_9s^9 \end{aligned} \tag{26}$$

TABLE I
STABILITY RANGES OF THE NUMBER OF GRID-CONNECTED INVERTERS

Time delay T_d (μs)	Stable ranges
30	$2N < 5.2$
	$2N > 61.5$
60	$2N < 3.1$
	$2N > 93.7$
75	$2N < 2.3$
	$2N > 105.4$

where a_i ($i = 0 \sim 9$) are shown in the Appendix due to space limitations.

According to the stability criterion, the grid-connected LSCPV system is stable only when the poles of the characteristic equation f(s) are located on the left half-plane. Based on (26), the root loci of the characteristic equation f(s) for time delays of 30, 60, and 75 μs are illustrated in Fig. 9.

As shown in Fig. 9, the poles gradually approach the imaginary axis and pass through it when the number of grid-connected inverters exceeds $2N_{1i}$ ($i = 3$, 6, and 7, where 3, 6, and 7 represent delays of 30, 60, and 75 μs, respectively). Meanwhile, as the number of grid-connected inverters continues to increase, the poles gradually begin to approach the imaginary axis and finally return to the left half-plane when the number of grid-connected inverters exceeds $2N_{2i}$ ($i = 3$, 6, 7). The pole position changes with the number of grid-connected inverters, which indicates that the system stability initially increases and then decreases as the number of grid-connected inverters increases. The poles are located in the left half-plane, which means that the grid-connected LSCPV system is only stable when the number of grid-connected inverters $2N$ satisfies $2N < 2N_{1i}$ or $2N > 2N_{2i}$ ($i = 3$, 6, 7).

It should be noted that the intersections of the root loci and the imaginary axis are the limits of the numbers of grid-connected inverters between which the system can work stably. Therefore, the stability ranges of the number of grid-connected inverters in Fig. 9 can be obtained, and they are listed in Table I according to (26). With increasing time delay, the stability range of the number of grid-connected inverters decreases significantly, which means that the allowable grid-connected capacity of LSCPV plants also decreases as the time delay increases.

C. Improved Capacitor-Current-Feedback Active Damping

As discussed in the previous section, the digitally controlled stability of the grid-connected LSCPV system is weakened by the digital time delay. Because many publications have focused on reducing or eliminating the effects of the time delay on the stability of digitally controlled grid-connected inverter systems [12]–[16] and considering the simplicity and effectiveness of the delay compensation method, a damping region extension method is proposed to increase the stability and robustness of the system. Moreover, for an LCL-type grid-connected inverter with capacitor-current feedback, the capacitor-current feedback is directly related to the damping region; thus, a wider damping region can be obtained by improving the capacitor-current feedback [14]–[17]. However, although the damping region has been efficiently extended using improved capacitor-current feedback in previous studies, the methods that were used were designed for cases in which the switching frequency is half of the sampling frequency; thus, the upper limit of the damping region only needs to be extended to approximately $0.25\,f_s$ since

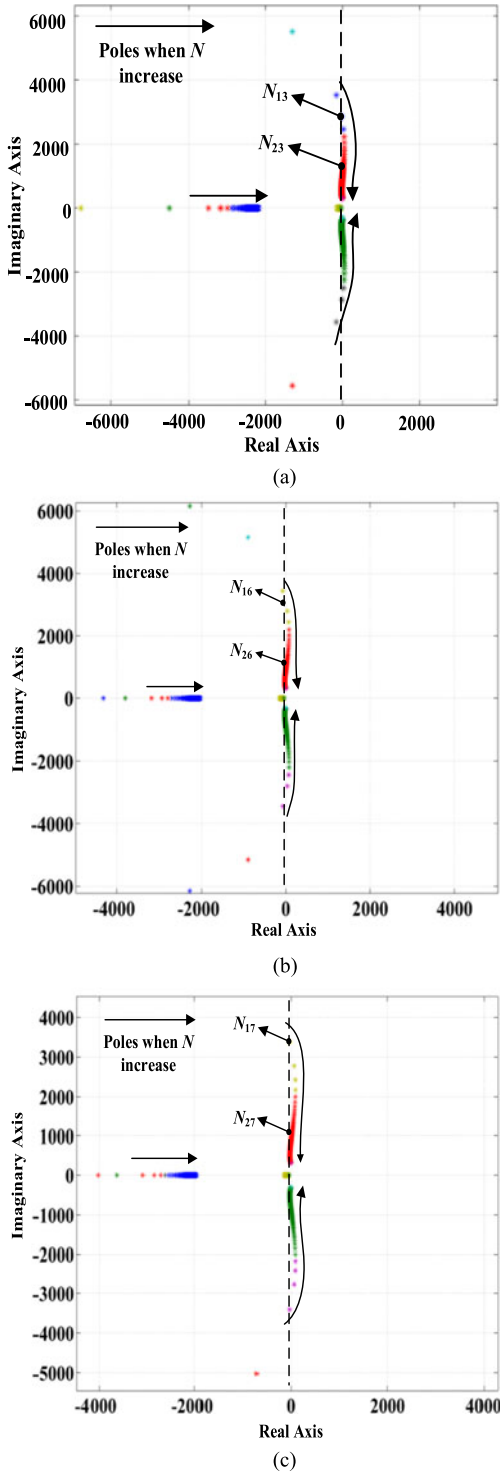

Fig. 9. Root loci of $f(s)$ with different time delays. (a) $T_{\rm d} = 30\,\mu$s. (b) $T_d = 60\,\mu$s. (c) $T_d = 75\,\mu$s.

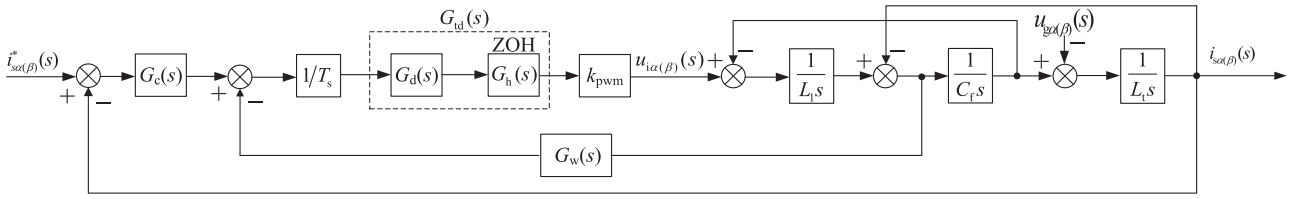

Fig. 10. Improved control loop of the grid-side inverter.

the LCL resonance frequency should be chosen to be between ten times the line frequency and one half of the switching frequency according to the LCL design criteria [27], [28]. Therefore, with an increase in the ratio of the switching frequency to the sampling frequency, the undamped region will increase or even account for half of the possible system resonance frequencies when the switching frequency is the same as the sampling frequency. Thus, the methods proposed in previous studies may not be sufficient to supply a sufficiently large damping region, which leaves the system vulnerable to instabilities due to shifting of the resonance frequency.

To address this issue, an improved capacitor-current feedback is required to expand the damping region in this case. As in the method described in [15], although the critical frequency increases as the order of the lead element increases, the system will become difficult to stabilize or even become unstable with the increase of the lead element order. Therefore, an improved capacitor-current-feedback method that considers the complexity of the system design and the increase of the critical frequency for the case that the switching frequency is the same as the sampling frequency is proposed to extend the damping region and increase the system stability for a larger ratio of the switching frequency to the sampling frequency. Fig. 10 shows the current control model with an improved capacitor-current feedback, where $L_t = L_2 + L_g$, and $G_w(s)$ is the feedback element of the capacitor current and can be expressed as

$$G_w(s) = \frac{k_d}{\left(\tau e^{-sT_s} + 1\right)^2}. \tag{27}$$

Taking $\tau = 0.8$ as an example, for the synchronous sampling case ($\lambda = 1$), based on the capacitor-current-feedback equivalent impedance $Z_{\rm eq}(s)$ defined in [16], the capacitor-current-feedback equivalent impedance of the improved capacitor-current feedback can be obtained as

$$Z_{\rm eq}(s) = \frac{L_1}{C_f k_{\rm pwm} G_{td}(s) G_w(s)} = R_d(\tau e^{-sT_s} + 1)^2 e^{1.5sT_s} \tag{28}$$

where $R_d = \frac{L_1}{k_{\rm pwm} C_f k_d}$. Substituting $s = j\omega$ into (28) yields

$$Z_{\rm eq}(j\omega) = R_{\rm eq}(\omega) + jX_{\rm eq}(\omega) \tag{29}$$

where

$$\begin{cases} R_{\rm eq}(\omega) = \cos 1.5\omega T_s + (\tau^2 + 2\tau)\cos(0.5\omega T_s) \\ X_{\rm eq}(\omega) = \sin 1.5\omega T_s + (-\tau^2 + 2\tau)\sin(0.5\omega T_s) \end{cases}. \tag{30}$$

According to (30), the boundary frequency at which $R_{\rm eq}$ becomes negative or positive is $0.37f_s$. The damping region will increase from $(0,\ f_s/6)$ to $(0,\ 0.37f_s)$, and thus the system robustness will increase [16].

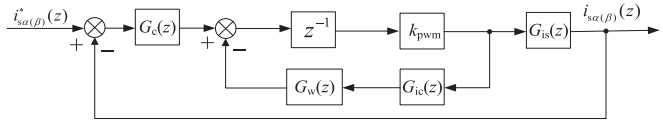

Fig. 11. Equivalent discrete model of the grid-connected inverter.

Based on Fig. 10, after applying the z transformation, the discrete-time domain control model of the single inverter is shown in Fig. 11, where

$$G_c(z) = k_p + \frac{2k_r\omega_i T_s(z-1)}{z^2 + (\omega_0^2 T_s^2 + 2\omega_i T_s - 2)z - 2\omega_i T_s + 1}$$

$$G_{\rm is}(z) = \frac{i_s(z)}{u_i(z)} = \frac{k_{\rm pwm}}{L_1 + L_t}\left[\frac{B\omega_{\rm re}T_s z - z(z-1)^2\sin(\omega_{\rm re}T_s)}{B\omega_{\rm re}z(z-1)}\right]$$

$$B = z^2 - 2z\cos(\omega_{\rm re}T_s) + 1,$$

$$G_{\rm ic}(z) = \frac{i_c(z)}{u_i(z)} = \frac{k_{\rm pwm}z(z-1)\sin(\omega_{\rm re}T_s)}{\omega_{\rm re}L_1 z[z^2 - 2z\cos(\omega_{\rm re}T_s) + 1]},$$

$$G_w(z) = \frac{k_d z^2}{(z+0.8)^2},$$

and $\omega_{\rm re} = \sqrt{(L_1 + L_t)/(L_1 L_t C_f)}$.

The open-loop transfer function of the system with the improved capacitor-current feedback can be obtained from Fig. 11 as

$$T(z) = \frac{G_c(z)L_1 k_{\rm pwm}[B\omega_{\rm re}T_s - (z-1)^2\sin\omega_{\rm re}T_s]}{(L_1 + L_t)(z-1)[B\omega_{\rm re}L_1 z + k_{\rm pwm}(z-1)G_w(z)\sin\omega_{\rm re}T_s]}. \tag{31}$$

According to Jury's criterion, when $G_c(z) = 1$, the case of the system without poles outside the unit circle can be obtained from (31) as follows:

$$\begin{cases} \left|1 - b_1^2\right| > |b_2 - b_1 b_4| \\ \left|(1-b_1^2)^2 - (b_2 - b_1 b_4)^2\right| > \left|(1-b_1^2)(b_3 - b_1 b_3)\right. \\ \qquad \left. - (b_4 - b_1 b_2)(b_2 - b_1 b_4)\right| \end{cases} \tag{32}$$

where $\delta = k_{\rm pwm}k_d\sin\omega_{\rm re}T_s/\omega_{\rm re}L_1$, $b_1 = 0.64$, $b_2 = 1.6 - \delta\sin(\omega_{\rm re}T_s) - 1.28\cos(\omega_{\rm re}T_s)$, $b_3 = \delta\sin(\omega_{\rm re}T_s) - 3.2\cos(\omega_{\rm re}T_s) + 1.64$, and $b_4 = 1.6 - 2\cos(\omega_{\rm re}T_s)$. Thus,

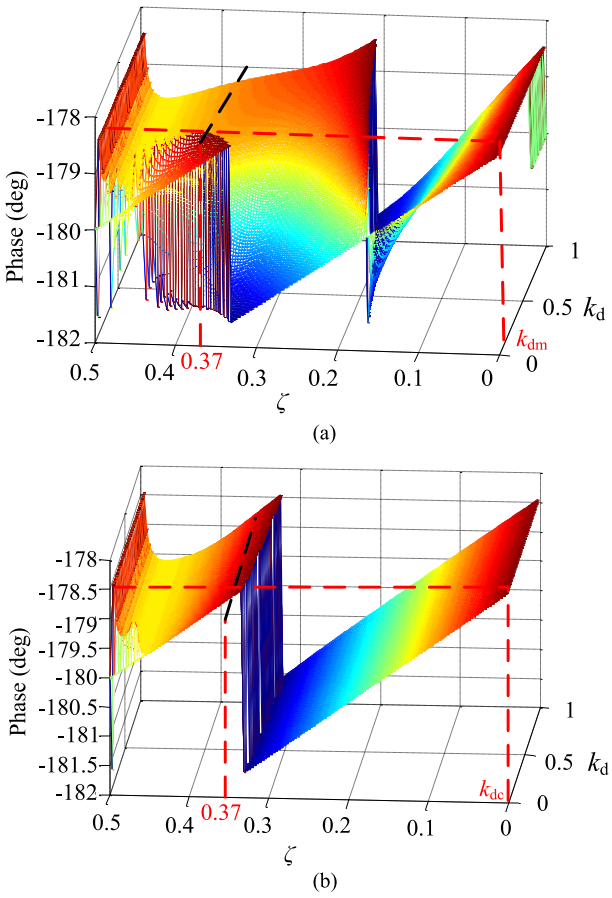

Fig. 12. Relationship between $\angle T(j\omega)$, ζ and k_d. (a) $f_{\rm re} < 0.37f_s$. (b) $f_{\rm re} > 0.37f_s$.

the stability range of k_d can be obtained from (32) with the designed resonant angular frequency.

Furthermore, according to the Nyquist stability criterion, in addition to considering the location of the open-loop poles in the analysis of the system stability, the number of $-180°$ crossings of $T(z)$ should also be investigated [12], [15], [16]. Therefore, with a series of equivalent transformations for (31), where $G_c(z)$ is simplified as k_p and z is substituted by $e^{j\omega T_s}$ [12], the phase of $T(z)$ can be derived as

$$\angle T(j\omega) = \operatorname{actan}\frac{c_1 e_2 - c_2 e_1}{c_1 e_1 + c_2 e_2} - \pi \tag{33}$$

where c_1, c_2, e_1, and e_2 are listed in the Appendix because of space limitations.

Fig. 12 shows the relationships between $\angle T(z)$, ζ, and k_d for two cases: $f_r < 0.37f_s$ and $f_r > 0.37f_s$, where ζ ($0<\zeta<1$) is the ratio between the system resonance frequency f_r and the sampling frequency f_s, and k_{dm} represents the upper limit of k_d. As shown in Fig. 12(a), when $f_r < 0.37f_s$ and $0 < k_d < k_{dm}$, the $-180°$ crossings occur at $f_s/6$, the left side of $0.37f_s$ and $0.5f_s$. However, when $k_d > k_{dm}$, the $-180°$ crossings only occur at $f_s/6$ and $0.5f_s$. In the case of $f_r > 0.37f_s$, there is also a critical value of k_d, which is denoted by $k_{\rm dc}$ in Fig. 12(b) and can be obtained by solving (33). When $0 < k_d < k_{\rm dc}$, there are

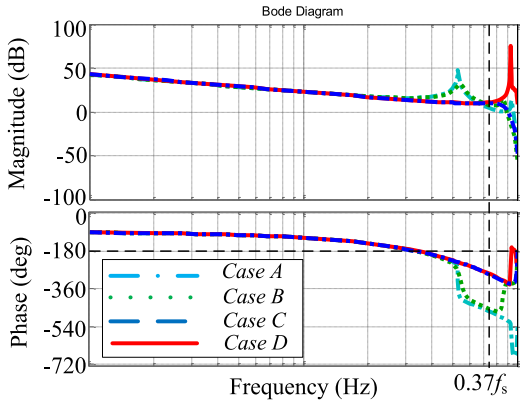

Fig. 13. Bode plots of $T(z)$ for four cases.

four $-180°$ crossings in the system: one at $f_s/6$, two between $0.37f_s$ and $0.5f_s$, and one at $0.5f_s$. If $k_d > k_{\rm dc}$, the $-180°$ crossings only occur at $f_s/6$ and $0.5f_s$.

Based on the previous analysis, four cases of the inverter with the improved capacitor-current feedback can be summarized as follows: *Case A*: $f_{\rm re} < 0.37f_s$, $0 < k_d < k_{dm}$; *Case B*: $f_{\rm re} < 0.37f_s$, $k_d > k_{dm}$; *Case C*: $f_{\rm re} > 0.37f_s$, $0 < k_d < k_{\rm dc}$; and *Case D*: $f_{\rm re} > 0.37f_s$, $k_d > k_{\rm dc}$. To analyze the system stability for the four cases more intuitively, the Bode plots of $T(z)$ for the four cases are shown in Fig. 13 based on (31). Without considering the $-180°$ crossing at the Nyquist frequency, for *Case B* and *Case D*, only one $-180°$ crossing exists in the system at $f_s/6$. For *Case A*, two $-180°$ crossings occur: one at $f_s/6$ and another on the right side of $0.37f_s$. For *Case* C, there are three $-180°$ crossings: one at $f_s/6$ and two between $0.37f_s$ and $0.5f_s$. Therefore, according to the Nyquist stability criterion and the previous analysis of the open-loop poles for different cases, the systems in *Case B* and *Case D* cannot reach stability due to the existence of a pair of open-loop unstable poles. The stability conditions of the systems in *Case A* and *Case C* can be derived as follows:

$$\begin{cases} \text{CaseA}: \\ \qquad \left|T(z=e^{j\omega_c T_s})\right| < 1 \text{and} \left|T(z=e^{j\omega_{c2} T_s})\right| < 1 \\ \text{CaseC}: \\ \qquad \left|T(z=e^{j\omega_c T_s})\right| < 1, \left|T(z=e^{j\omega_{c2} T_s})\right| > 1 \\ \qquad \text{and} \left|T(z=e^{j\omega_{c3} T_s})\right| < 1 \end{cases} \tag{34}$$

where ω_c is the cutoff angular frequency, and ω_{c2} and ω_{c3} represent the angular frequencies of the second and third $-180°$ crossings, respectively, which are located between $0.37f_s$ and $0.5f_s$.

The stability ranges obtained by the preceding method for the number of grid-connected inverters in the grid-connected LSCPV system with the improved capacitor-current feedback are shown in Table II. Compared with the stability ranges of the number of grid-connected inverters for the system with the conventional capacitor-current feedback, which are shown in Table I, the stability ranges for the system with the improved capacitor-current feedback expand as the system stability increases.

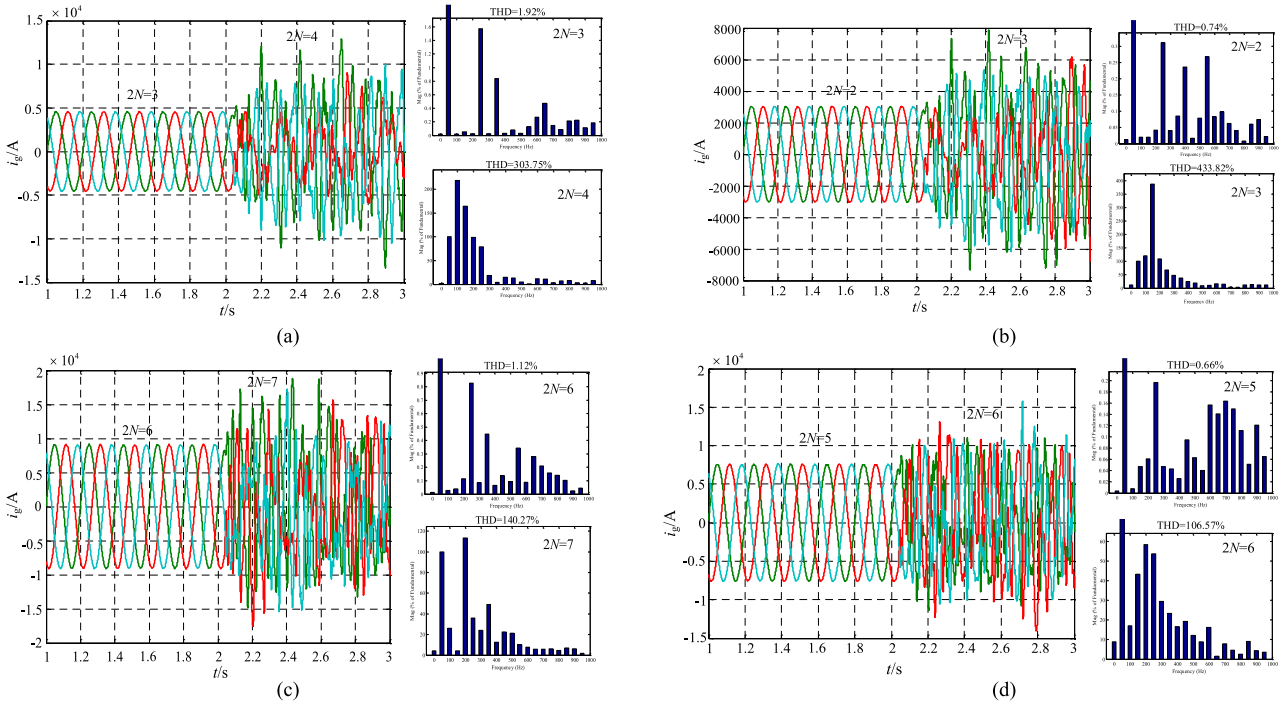

Fig. 14. Simulation waveforms of the grid current i_g and its FFT analysis. (a) System with the conventional capacitor-current feedback and a time delay of 60 μs. (b) System with the conventional capacitor-current feedback and a time delay of 75 μs. (c) System with the improved capacitor-current feedback and a time delay of 60 μs. (d) System with the improved capacitor-current feedback and a time delay of 75 μs.

TABLE II
STABILITY RANGES OF THE NUMBER OF GRID-CONNECTED INVERTERS WITH THE IMPROVED CAPACITOR-CURRENT FEEDBACK

Time delay T_d (μs)	Stable ranges
30	$2N < 7.9$
	$2N > 30.5$
60	$2N < 6.1$
	$2N > 58.3$
75	$2N < 5.6$
	$2N > 76.4$

TABLE III
MAIN PARAMETERS OF THE GRID-CONNECTED INVERTER

Quantity	Notation	Value
Line voltage	u_g	270 V $_{(\mathrm{rms})}$
DC-side voltage	V_{dc}	720 V
Line frequency	f_0	50 Hz
Rated power	P	500 kW
Grid side filter inductance	L_2	11 μH
Inverter side filter inductance	L_1	66 μH
Filter capacitance	C_f	548 μF

TABLE IV
MAIN PARAMETERS OF THE TRANSMISSION NETWORK

Component	Quantity	Notation	Value
	Short-circuit voltage (%)	$U_k\,\%$	10.5
Large capacity	Rated voltage of low-voltage side	U_l	10 kV
stepup transformer	Rated voltage of high-voltage side	U_h	110 kV
	Rated capacity	S	6300 kVA
Transmission Line	Resistance	r	0.21 Ω/km
	Reactance	x	0.34 Ω/km
	Line length	l	20 km

IV. SIMULATION AND EXPERIMENTAL RESULTS

A. Simulation Results

An equivalent grid-connected LSCPV system model with the improved capacitor-current feedback was built and tested in MATLAB/SIMULINK to validate the theoretical analysis and the obtained stability ranges of the number of grid-connected inverters. The main parameters of the system are listed in Tables III and IV.

According to (5), the equivalent impedance of the transmission network is

$$\begin{cases} L_g = (3.87 + 15.78)\mu\mathrm{H} = 19.65\ \mu\mathrm{H} \\ R_g = 3.1\ \mathrm{m}\Omega \end{cases}. \tag{35}$$

The equivalent inductance of the 10 kV split-winding transformer is equal to its low-voltage windings leakage inductance value, which is 10.4 μH. Based on Table II, when the time delay T_d is 60 μs, the grid-connected system is stable only when the number of grid-connected inverters ($2N$) satisfies $2N < 6.1$ or $2N > 58.3$. When the time delay T_d is 75 μs, the stability range of the number of grid-connected inverters is $2N < 5.6$ or $2N > 76.4$. Because the simulation is tedious if the number of inverters is large, only $2N < N_{1i}$ ($i = 6, 7$) is considered in the simulation and the experiment. Moreover, since working in the damping region is essential to obtaining a

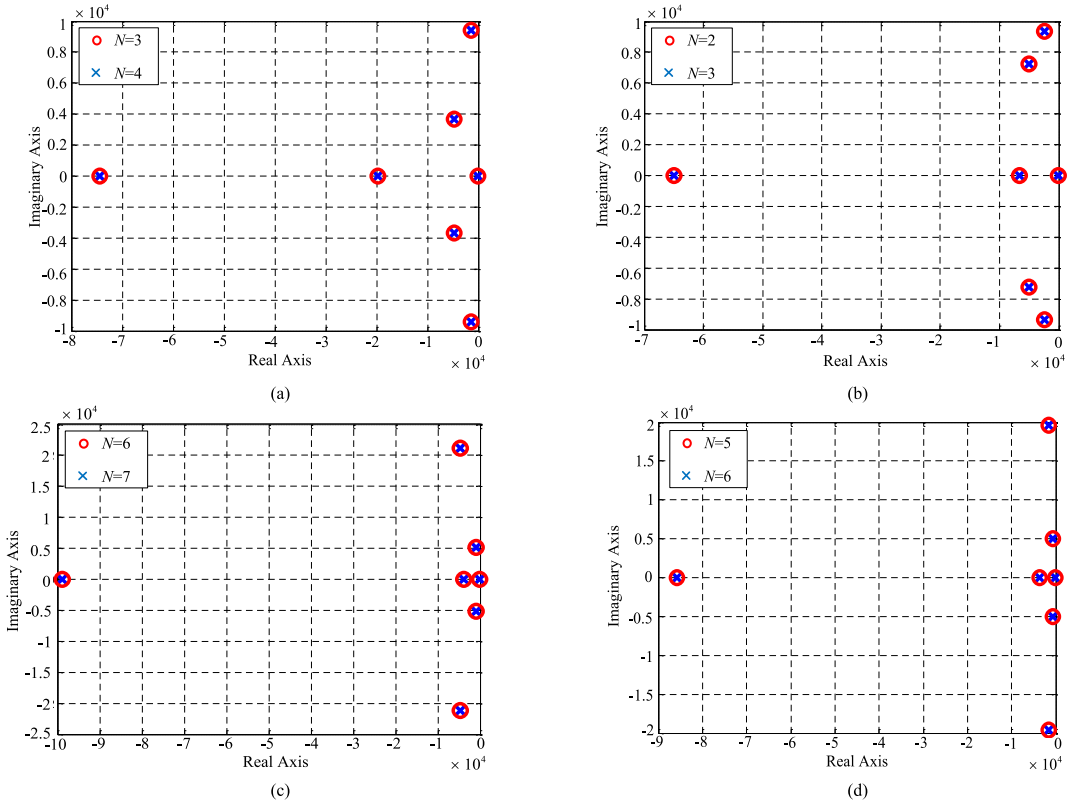

Fig. 15. Pole maps of the equivalent reference current i_{pv}. (a) System with the conventional capacitor-current feedback and a time delay of 60 μs. (b) System with the conventional capacitor-current feedback and a time delay of 75 μs. (c) System with the improved capacitor-current feedback and a time delay of 60 μs. (d) System with the improved capacitor-current feedback and a time delay of 75 μs.

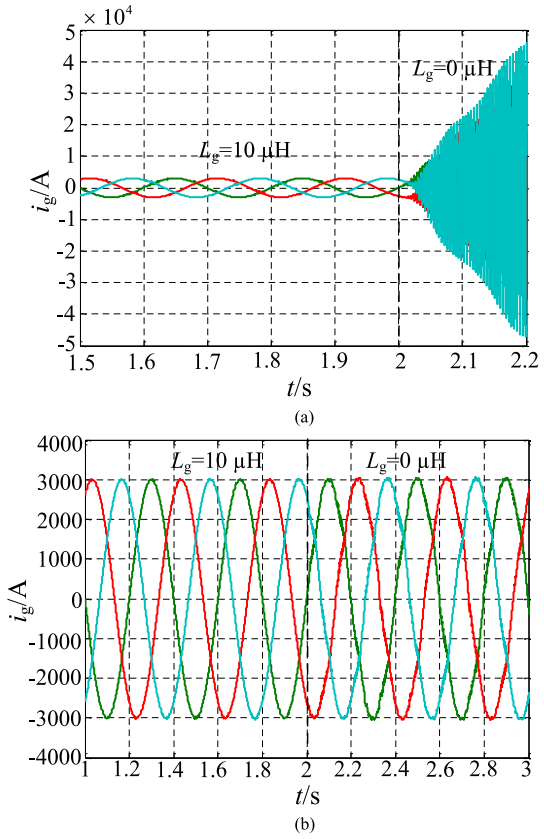

Fig. 16. Simulation waveforms of the grid current i_g with varying grid impedances at 2 s. (a) System with the conventional capacitor-current feedback. (b) System with the improved capacitor-current feedback.

Fig. 17. Main experimental setup.

higher-quality output current and making the system easier to stabilize, the system is designed to work in its damping region; thus, with the stability requirements in (32) and (34), the proportional coefficient k_p and active damping coefficient k_d are obtained as 0.72 and 0.2, respectively.

To demonstrate the superior performance of the proposed delay compensation method, Fig. 14 shows the waveforms of the grid current i_g, which can be considered the output current of the entire grid-connected LSCPV system, and its fast Fourier transformation (FFT) analysis for time delays of 60 and 75 μs in two systems: the system with the conventional capacitor-current feedback and the system with the improved

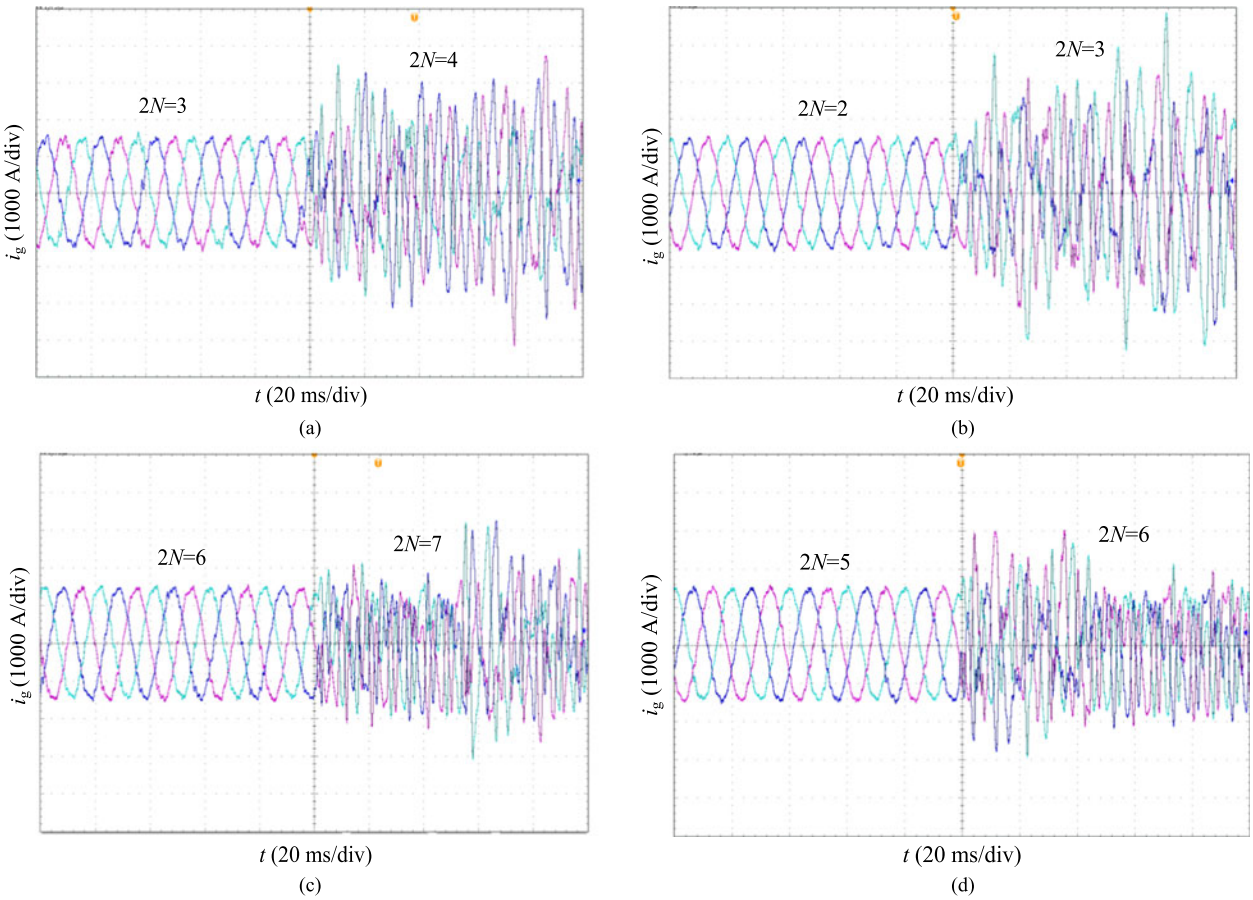

Fig. 18. Experimental waveforms of the grid current i_g. (a) System with the conventional capacitor-current feedback and a time delay of 60 μs. (b) System with the conventional capacitor-current feedback and a time delay of 75 μs. (c) System with the improved capacitor-current feedback and a time delay of 60 μs. (d) System with the improved capacitor-current feedback and a time delay of 75 μs.

capacitor-current feedback. The grid current i_g is stable only when the number of grid-connected inverters is within its stability range, and there is a wider stability range for the number of grid-connected inverters in the system with a time delay T_d of 60 μs. In addition, the system with the improved capacitor-current feedback remains stable with more inverters than the system with the traditional capacitor-current feedback, which validates the effectiveness and advantages of the method proposed in Section III. Fig. 15 shows the pole maps of (15) for the case shown in Fig. 14. As seen, the poles are located in the left plane, which indicates that the equivalent reference current ($i_{\rm pv}$) is stable in all of these situations. As discussed in Section III, the off-grid LSCPV plant is stable only when each inverter in the plant is stable, and the stability of the equivalent reference current of the inverter ($i_{\rm pv}$) is the key to inverter stability in the off-grid LSCPV plant. Thus, the results shown in Fig. 15 are consistent with the assumption that the LSCPV plant itself is stable even when the entire system is unstable.

Furthermore, as was discussed in previous studies, the system damping region is directly related to the stability and robustness of the grid-connected inverter system [14]–[18]. Therefore, for LSCPV plants, which primarily consist of inverters, the wider inverter damping region obtained from the proposed capacitor-current feedback will increase both the stability range of the number of grid-connected inverters and the system's robustness against variations in grid impedance. Fig. 16 shows the waveforms of i_g for two grid-connected inverters in two systems, and values of $L_2 = 1$ μH and $R_g = 0$ Ω are used to change the system resonance frequency from 2214 Hz ($< f_s/6$) to 6850 Hz ($< 0.37 f_s$) with a change in the grid inductance (L_g) from 10 to 0 μH at 2 s. Fig. 16(a) shows that i_g becomes unstable when the system resonance frequency is higher than its critical frequency, which is $f_s/6$ in the system with the conventional capacitor-current feedback. However, in the system with the improved capacitor-current feedback, the grid current i_g remains stable and maintains a better quality even when the system resonance frequency of the inverter is considerably higher than $f_s/6$. A wider damping region in the system with the improved capacitor-current feedback is verified to provide the system with satisfactory damping performance, which is essential to obtaining a better quality output current and higher robustness against variations in grid impedance.

B. Experimental Results

Experiments were conducted on a three-phase inverter system. Fig. 17 shows the main experimental setup, which comprises a three-phase inverter, a dc distribution and other additional circuits. An ac distribution is used to simulate the grid-side voltage to reduce the influence on the real grid, and

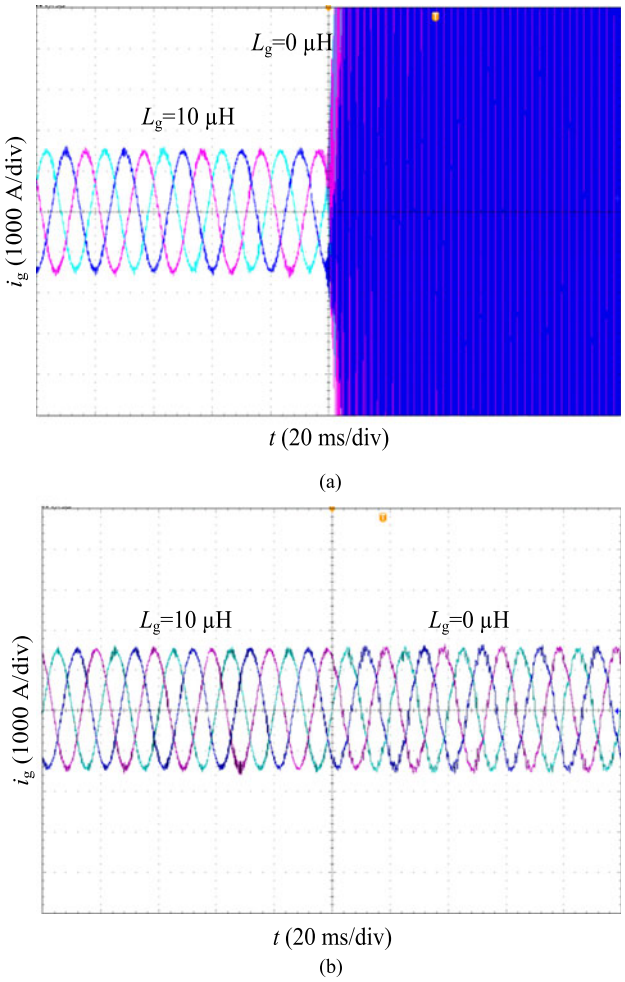

Fig. 19. Experimental waveforms of the grid current i_g with varying grid impedances. (a) System with the conventional capacitor-current feedback. (b) System with the improved capacitor-current feedback.

the transformer and transmission line are equivalent to the impedance given in (35). In contrast to the equivalent model of the grid-connected LSCPV system, which contains numerous inverters, because an LSCPV plant that contains numerous large capacity inverters is difficult to construct in the laboratory, 2*N* times the equivalent impedance is used instead of increasing the number of grid-connected inverters 2*N* [4], [9], [19].

Fig. 18 shows the experimental waveforms of the grid current for time delays of 60 and 75 μs in the system with the conventional capacitor-current feedback and the system with the improved capacitor-current feedback. Because the increased number of grid-connected inverters is replaced by an increased impedance, under the operational model with constant output power, the magnitudes of the grid current remain nearly constant when the system is stable because the grid voltage remains steady. Moreover, when the number of grid-connected inverters increases beyond its stability range, the grid current becomes unstable, which verifies that the stability range of the number of grid-connected inverters decreases as the time delay increases and expands with the proposed damping region extension method. These trends indicate that the system with the improved capacitor-current feedback can be stable with a larger number of grid-connected inverters since the system stability was considerably better with the proposed method.

Fig. 19 shows the experimental waveforms of the grid current with $T_d = 75\,\mu$s, $R_g = 0\,\Omega$ and $L_2 = 1\,\mu$H, and varying grid impedance from 10 to 0 μH in the system with the conventional capacitor-current feedback and the system with the proposed method. When L_g decreased to 0 μH, i_g becomes unstable in the system with the conventional capacitor-current feedback but remains stable in the system with the proposed method, which verifies that the system with the improved active damping loop can obtain a wider damping region and simultaneously retain a satisfactory output current quality.

V. Conclusion

This paper presents a detailed process for the development of a digitally controlled grid-connected LSCPV system model and obtains an equivalent Norton model of the grid-connected LSCPV system. The effects of time delays on the stability of grid-connected LSCPV systems are discussed based on the model and the impedance-based criterion. The influence of the time delay on the stability range of the number of grid-connected inverters is determined by the root locus, and the stability range of the number of grid-connected inverters is obtained. To improve the system stability, a delay compensation method is proposed to extend the system damping region, which is reduced by the time delay. Simulation and experimental results validate the analysis of the effects of the time delay on the grid-connected LSCPV system and the calculated stability range of the grid-connected inverter.

The influence of time delays on grid-connected LSCPV systems was comprehensively explored using a model of a digitally controlled grid-connected LSCPV system in the *s*-domain, and the results and the applied analysis method are helpful for analyzing and designing digitally controlled grid-connected LSCPV systems. However, a more accurate *z*-domain model may be needed for further analysis of the stability of the digitally controlled grid-connected LSCPV system, and additional experiments in actual grid-connected LSCPV system are required to verify the theoretical analysis and the obtained stability range of the grid-connected capacity of the LSCPV plant. Moreover, although the system damping region was extended to $(0, 0.37f_s)$ by the proposed method, a region of $(0.37f_s, 0.5f_s)$ that is not covered by the damping region still exists when the sampling frequency is equal to the switching frequency. Therefore, an improved delay compensation method is a future direction of research.

Appendix

According to (26), the coefficients of *f*(*s*) can be obtained using Mathematica and are: $a_0 = (24N + 12k_pk_{\mathrm{pwm}})\omega_0^2$

$$\begin{aligned} a_1 = {} & 12L_TR_g\omega_0^2 + 48N\omega_c + 24Nk_dk_{\mathrm{pwm}}C_f\omega_0^2 \\ & + 24NT_s\omega_0^2 - 6k_{\mathrm{pwm}}T_sk_p\omega_0^2R_g + 24k_{\mathrm{pwm}}\omega_ck_pL_g \\ & + 12k_{\mathrm{pwm}}k_p\omega_0^2L_g + 24k_{\mathrm{pwm}}k_r\omega_cR_g \end{aligned}$$

$$
\begin{aligned}
a_2 = {} & [(12k_d k_{\mathrm{pwm}} C_f \omega_0^2 R_g + 12T_s \omega_0^2 R_g)(L_T + L_2) \\
& + (24k_{\mathrm{pwm}} \omega_c L_g - 12k_{\mathrm{pwm}} T_s \omega_c R_g)(k_p + k_r) \\
& + 24L_T R_g \omega_c + 12L_T T_s R_g \omega_0^2 + 12L_T L_g \omega_0^2 + 24N \\
& + 48Nk_d k_{\mathrm{pwm}} C_f \omega_c + 48NT\omega_c - 12Nk_d k_{\mathrm{pwm}} C_f T_s \omega_0^2 \\
& + 8NT_s^2 \omega_0^2 + 24NL_1 C_f \omega_0^2 + k_{\mathrm{pwm}} T_s^2 k_p \omega_0^2 R_g \\
& - 6k_{\mathrm{pwm}} T_s k_p \omega_0^2 L_g + 12k_{\mathrm{pwm}} k_p R_g] \\
a_3 = {} & [(4T_s^2 \omega_0^2 R_g + 24T_s \omega_c R_g + 12T_s \omega_0^2 L_g)(L_1 + L_2) \\
& + (2k_{\mathrm{pwm}} T_s^2 \omega_c R_g - 12\omega_c k_{\mathrm{pwm}} T_s L_g)(k_p + k_r) \\
& + 12L_T R_g + 24L_T T_s R_g \omega_c + 24L_T L_g \omega_c \\
& + 24L_T k_d k_{\mathrm{pwm}} C_f \omega_c R_g + 12L_1 L_T C_f R_g \omega_0^2 \\
& + 4L_T T_s^2 R_g \omega_0^2 + 12L_T T_s L_g \omega_0^2 - 6L_T k_d k_{\mathrm{pwm}} \\
& C_f T_s \omega_0^2 R_g + 24Nk_d k_{\mathrm{pwm}} C_f + 24NT_s - 24Nk_d k_{\mathrm{pwm}} \\
& T_s C_f \omega_c + 16NT_s^2 \omega_c + 48NL_1 C_f \omega_c + 2Nk_d k_{\mathrm{pwm}} \\
& T_s^2 C_f \omega_0^2 + NT_s^3 \omega_0^2 + 24NL_1 C_f T_s \omega_0^2 + 12k_d k_{\mathrm{pwm}} \\
& L_2 C_f \omega_0^2 L_g + + k_{\mathrm{pwm}} T_s^2 k_p \omega_0^2 L_g - 6k_{\mathrm{pwm}} T_s k_p R_g \\
& + 12k_{\mathrm{pwm}} k_p L_g + 12L_T k_d k_{\mathrm{pwm}} C_f \omega_0^2 L_g] \\
a_4 = {} & [(0.5T_s^3 R_g \omega_0^2 + 8T_s^2 R_g \omega_c + 4T_s^2 L_g \omega_0^2 \\
& + 24T_s L_g \omega_c)(L_1 + L_2 + L_T) + 12L_1 C_f T_s \omega_0^2 R_g \\
& (L_2 + L_T)12L_T T_s R_g + 12T_s R_g (L_1 + L_2) + 12L_T L_g \\
& + 12L_T k_d k_{\mathrm{pwm}} C_f R_g + 24L_1 L_T C_f R_g \omega_c \\
& + 8NT_s^2 - 12L_T k_d k_{\mathrm{pwm}} C_f T_s \omega_c R_g \\
& + 12L_1 L_T C_f T_s R_g \omega_0^2 + L_T k_d k_{\mathrm{pwm}} C_f T_s^2 \omega_0^2 R_g \\
& - 12Nk_d k_{\mathrm{pwm}} C_f T_s + 24NL_1 C_f + 4Nk_d k_{\mathrm{pwm}} T_s^2 C_f \omega_c \\
& + 2NT_s^3 \omega_c + 48NL_1 C_f T_s \omega_c + 8NL_1 C_f T_s^2 \omega_0^2 \\
& + 12k_d k_{\mathrm{pwm}} L_2 C_f R_g - 6k_d k_{\mathrm{pwm}} L_2 T_s C_f R_g \omega_c \\
& + k_p k_{\mathrm{pwm}} T_s^2 R_g + 2k_{\mathrm{pwm}} T_s^2 \omega_c L_g (k_p + k_r) \\
& - 6k_{\mathrm{pwm}} T_s k_p L_g + 24L_T k_d k_{\mathrm{pwm}} C_f \omega_c L_g \\
& - 6L_T k_d k_{\mathrm{pwm}} T_s C_f L_g \omega_0^2] \\
a_5 = {} & [(4T_s^2 R_g + 12T_s L_g + 8T_s^2 L_g \omega_c + 0.5T_s^3 L_g \omega_0^2 \\
& + T_s^3 R_g \omega_c)(L_1 + L_2 + L_T) + (4L_1 L_2 C_f T_s^2 \omega_0^2 R \\
& + 24L_1 C_f T_s \omega_c R_g + 12L_1 C_f T \omega_0^2 L_g - 6k_d k_{\mathrm{pwm}} \\
& \times C_f T_s R_g + 2k_d k_{\mathrm{pwm}} C_f T_s^2 \omega_c R_g)(L_2 + L_T) \\
& + 12L_T k_d k_{\mathrm{pwm}} C_f L_g (T_s - 1) + 12L_1 L_T C_f R_g \\
& + 24L_1 L_T C_f T_s \omega_c L_g + 12L_1 L_T C_f T \omega_0^2 R_g \\
& + 2Nk_d k_{\mathrm{pwm}} T_s^2 C_f + NT_s^3 + L_T k_d k_{\mathrm{pwm}} T_s^2 C_f L_g \omega_0^2 \\
& + 24NL_1 C_f T_s + 16NL_1 C_f T_s^2 \omega_c + NL_1 C_f T_s^3 \omega_0^2 \\
& + 12k_d k_{\mathrm{pwm}} L_2 C_f L_g - 6k_d k_{\mathrm{pwm}} L_2 C_f T_s \omega_c L_g \\
& + k_d k_{\mathrm{pwm}} T_s^2 L_g] \\
a_6 = {} & [(0.5T_s^3 R_g + 4T_s^2 L_g + T_s^3 L_g \omega_c)(L_1 + L_2 + L_T) \\
& + (k_d k_{\mathrm{pwm}} C_f T_s^2 R_g + 8L_1 C_f T_s^2 R_g \omega_c \\
& + 24L_1 C_f T_s \omega_c L_g - 6k_d k_{\mathrm{pwm}} C_f T_s L_g \\
& + 2k_d k_{\mathrm{pwm}} C_f T_s^2 L_g \omega_c + 12L_1 C_f T_s R_g)(L_2 + L_T) \\
& + 12L_1 L_T C_f L_g + 8L_1 L_2 C_f T_s^2 L_g \omega_0^2 + 8NL_1 C_f T_s^2 \\
& + 2NL_1 C_f T_s^3 \omega_c + 0.5L_1 L_2 C_f T_s^3 \omega_0^2 R_g] \\
a_7 = {} & [0.5T_s^3 L_g (L_1 + L_2 + L_T) + (4L_1 C_f T_s^2 R_g + 12L_1 C_f T_s L_g \\
& + L_1 C_f T_s^3 R_g \omega_c + 0.5L_1 C_f T_s^3 L_g \omega_0^2 + k_d k_{\mathrm{pwm}} \\
& \times C_f T_s^2 L_g)(L_2 + L_T) + 16L_1 L_2 C_f T_s^2 \omega_c L_g \\
& + NL_1 C_f T_s^3], \ \textit{and} \\
a_8 = {} & [(0.5L_1 C_f T_s^3 R_g + L_1 C_f T_s^3 L_g \omega_c)(L_2 + L_T) \\
& + 8L_1 L_2 C_f T_s^2 L_g], \quad a_9 = 0.5L_1 C_f T_s^3 L_g (L_2 + L_T).
\end{aligned}
$$

The coefficients in (33) are listed as follows:

$$
\begin{aligned}
c_1 = {} & \cos(6\omega T_s) + (b_4 - 1)\cos(5\omega T_s) + \\
& (b_3 - b_4)\cos(4\omega T_s) + (b_2 - b_3)\cos(3\omega T_s) \\
& + (b_1 - b_2)\cos(2\omega T_s) - b_1 \cos(\omega T_s) \\
c_2 = {} & \sin(6\omega T_s) + (b_4 - 1)\sin(5\omega T_s) + \\
& (b_3 - b_4)\sin(4\omega T_s) + (b_2 - b_3)\sin(3\omega T_s) \\
& + (b_1 - b_2)\sin(2\omega T_s) - b_1 \sin(\omega T_s) \\
d_1 = {} & \cos(4\omega T_s) + b_4 \cos(3\omega T_s) + \\
& (b_3 - \delta)\cos(2\omega T_s) + (b_2 + \delta)\cos(\omega T_s) \\
d_2 = {} & \sin(4\omega T_s) + b_4 \sin(3\omega T_s) + (b_3 - \delta)\sin \\
& (2\omega T_s) + (b_2 + \delta)\sin(\omega T_s) \\
d_3 = {} & \cos(4\omega T_s) - 0.4\cos(3\omega T_s) - 1.56\cos(2\omega T_s) \\
& + 0.96\cos(\omega T_s) + 0.64 \\
d_4 = {} & \sin(4\omega T_s) - 0.4\sin(3\omega T_s) \\
& - 1.56\sin(2\omega T_s) + 0.96\cos(\omega T_s) \\
e_1 = {} & \omega_{\mathrm{re}} T_s d_1 - d_3 \sin(\omega_{\mathrm{re}} T_s)
\end{aligned}
$$

and $e_2 = \omega_{\mathrm{re}} T_s d_2 - d_4 \sin(\omega_{\mathrm{re}} T_s)$.

REFERENCES

[1] L. Asiminoaei, R. Teodorescu, F. Blaabjerg, and U. Borup, "Implementation and test of an online embedded grid impedance estimation technique for PV inverters," *IEEE Trans. Ind. Electron.*, vol. 52, no. 4, pp. 1136–1144, Aug. 2005.

[2] International Energy Agency, "PVPS report snapshot of global PV 1992–2013," Paris Cedex, France, Rep. IEA PVPS TI-24, 2014.

[3] S. Kouro, J. I. Leon, and L. G. Franquelo, "Grid-connected photovoltaic systems: An overview of recent research and emerging PV converter technology," *IEEE Ind. Electron. Mag.*, vol. 9, no. 1, pp. 47–61, Mar. 2015.
[4] L. Zhou and M. Zhang, "Modeling and stability of large-scale PV plants due to grid impedance," in *Proc.IEEE 39th Annu. Conf. Ind. Electron. Soc.*, Vienna, Austria, Nov. 2013, pp. 1025–1030.
[5] W. Li, D. Pan, X. Ruan, and X. Wang, "A full-feedforward scheme of grid voltages for a three-phase grid-connected inverter with an LCL filter," in *Proc. Energy Convers. Congr. Expo.*, Phoenix, AZ, USA, Sep. 2011, pp. 96–103.
[6] J. Sun, "Impedance-based stability criterion for grid-connected inverters," *IEEE Trans. Power Electron.*, vol. 26, no. 11, pp. 3075–3078, Nov. 2011.
[7] J. W. He, Y. W. Li, D. Bosnjak, and B. Harris, "Investigation and resonances damping of multiple PV inverters," in *Proc. IEEE Appl. Power Electron. Conf. Expo.*, Orlando, FL, USA, Feb. 2012, pp. 246–253.
[8] Z. Zou, Z. Wang, and M. Cheng, "Modeling, analysis, design of multifunction grid-interfaced inverters with output LCL filter," *IEEE Trans. Power Electron.*, vol. 29, no. 7, pp. 3830–3839, Jul. 2014.
[9] T. B. Lazzarin, G. A. T. Bauer, and I. Barbi, "A control strategy for parallel operation of single-phase voltage source inverters: Analysis, design and experimental results," *IEEE Trans. Ind. Electron.*, vol. 60, no. 6, pp. 2194–2204, Jun. 2013.
[10] J. He and Y. W. Li, "Generalized closed-loop control schemes with embedded virtual impedances for voltage source converters with LC or LCL filters," *IEEE Trans. Power Electron.*, vol. 27, no. 4, pp. 1850–1861, Apr. 2012.
[11] X. Zhang, J. W. Spencer, and J. M. Guerrero, "Small-signal modeling of digitally controlled grid-connected inverters with LCL filters," *IEEE Trans. Ind. Electron.*, vol. 60, no. 9, pp. 3752–3765, Sep. 2013.
[12] J. G Wang, J. D. Yan, L. Jiang, and J. Zou, "Delay-dependent stability of single-loop controlled grid-connected inverters with LCL filters," *IEEE Trans. Power Electron.*, vol. 31, no. 1, pp. 743–757, Jan. 2016.
[13] V. Miskovic, V. Blasko, T. M. Jahns, A. H. C. Smith, and C. Romenesko, "Observer based active damping LCL resonance in grid-connected voltage source converters," *IEEE Trans. Ind. Appl.*, vol. 50, no. 6, pp. 3977–3985, Nov./Dec. 2010.
[14] Z. Xin, X. F. Wang, P. C. Loh, and F. Blaabjerg, "Grid-current feedback control for LCL-filter grid converters with enhanced stability," *IEEE Trans. Power Electron.*, vol. 32, no. 4, pp. 3216–3228, Apr. 2017, doi: 10.1109/TPEL. 2016. 2580543.
[15] X. Q. Li, X. J. Wu, Y. W. Geng, X. B. Yuan, C. Y. Xia, and X. Zhang, "Wide damping region for LCL-type grid-connected inverter with an improved capacitor-current-feedback methos," *IEEE Trans Power Electron.*, vol. 30, no. 9, pp. 5247–5259, Sep. 2015.
[16] D. Pan, X. Runa, C. Bao, W. Li, and X. Wang, "Capacitor current feedback active damping with reduced computation delay for improving robustness of LCL-type grid-connected inverter," *IEEE Trans. Power Electron.*, vol. 29, no. 7, pp. 3404–3427, Jul. 2014.
[17] C. Bao, X. Ruan, X. Wang, W. Li, D. Pan, and K. Weng, "Step-by-step controller design for LCL-type grid-connected inverter with capacitor-current-feedback active-damping," *IEEE Trans. Power Electron.*, vol. 29, no. 3, pp. 1239–1253, Mar. 2014.
[18] S. G. Parker, B. P. McGrath, and D. G Holmes, "Regions of active damping control for LCL filters," *IEEE Trans. Ind. Appl.*, vol. 50, no. 1, pp. 424–432, Jan./Feb. 2014.
[19] R. Turner, S. Walton, and R. Duke, "Stability and bandwidth implications of digitally controlled grid-connected parallel inverters," *IEEE Trans. Ind. Electron.*, vol. 57, no. 11, pp. 3685–3694, Nov. 2010.
[20] Y. Zhang and H. Ma, "Theoretical and experimental investigation of networked control for parallel operation of inverters," *IEEE Trans. Ind. Electron.*, vol. 59, no. 4, pp. 1961–1970, Apr. 2012.
[21] J. He, Y. W. Li, D. Bosnjak, and B. Harris, "Investigation and active damping of multiple resonances in a parallel-inverter-based microgrid," *IEEE Trans. Power Electron.*, vol. 28, no. 1, pp. 234–246, Jan. 2013.
[22] T. Gönen, *Modern Power System Analysis*, 2nd ed. Boca Raton, FL, USA: CRC Press, 2013.
[23] W. G. Hurley and W. H. Wlfle, *Transformers and Inductors for Power Electronics: Theory, Design and Applications*. Hoboken, NJ, USA: Wiley, 2013.
[24] E. Figueres, G. Garcerá, J. Sandia, F. González-Espín, and J. C. Rubio, "Sensitivity study of the dynamics of three-phase photovoltaic inverters with and LCL grid filter," *IEEE Trans. Ind. Electron.*, vol. 56, no. 3, pp. 706–717, Mar. 2009.
[25] S. Buso and P. Mattavelli, *Digital Control in Power Electronics*. Ft. Collins, CO, USA: Morgan & Claypool, 2006.
[26] S. V. Kulkarni and S. A. Khaparde, *Transformer Engineering: Design and Practice*. New York, NY, USA: Marcel Dekker, May 2004.
[27] A. Reznik, M. Simoes, A. Al-Durra, and S. Muyeen, "LCL filter design and performance analysis for grid-interconnected systems," *IEEE Trans. Ind. Appl.*, vol. 50, no. 2, pp. 1225–1232, Mar./Apr. 2014.
[28] R. Pena-Alzola, M. Liserre, F. Blaabjerg, M. Ordonez, and Y. Yang, "LCL-filter design for robust active damping in grid connected converters," *IEEE Trans. Ind. Informat.*, vol. 10, no. 4, pp. 2192–2203, Nov. 2014.

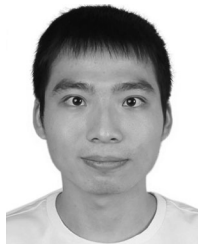

Jinhong Liu was born in Changde, China, in 1989. He received the B.S. degree in electrical engineering from Hunan University of Science and Technology, Xiangtan, China, in 2011, and is currently working toward the Ph.D. degree in electrical engineering from Chongqing University, Chongqing, China.

His current research interests include grid-connected photovoltaic system and digital controller.

Lin Zhou was born in Sichuan Province, China, in 1961. He received the B.S. degree in electrical engineering, in 1984, the M.S. degree in electrical engineering from the Department of Electrical Engineering, in 1988, and the Ph.D. degree in electrical engineering from the Department of Electrical Engineering in 2004, all from Chongqing University, Chongqing, China.

From December 2008 to December 2009, he was a Visiting Scholar in Durham University, Durham, U.K., where he was engaged in researching on microgrid and renewable energy generation. He is currently a Professor in the State Key Laboratory of Transmission and Distribution Equipment and Power System Safety and New Technology, Chongqing University. He is engaged in teaching and scientific research of power electronic technology and power system. His other research interests include key technology of distributed generation and power quality control.

Bin Li received the M.S. degree in control theory and control engineering both from Henan Polytechnic University, Henan, China, in 2013. He is currently working toward the Ph.D. degree in electrical engineering from Chongqing University, Chongqing, China.

His current research interests include inverter control for distributed generator and virtual synchronous generator for the distributed generator.

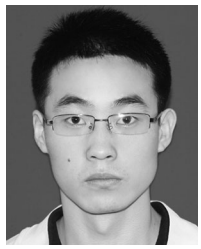

Chen Zheng received the B.S. degree in electrical engineering from Henan Polytechnic University, Jiaozuo, China, in 2013. He is currently working toward the Ph.D. degree in electrical engineering at Chongqing University, Chongqing, China.

His current research interest includes key technology of photovoltaic power system.

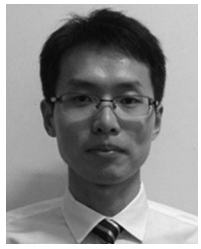

Bao Xie received the B.S. degree in electrical engineering from Chongqing University, Chongqing, China, in 2014. He is currently working toward the Ph.D. degree in electrical engineering at Chongqing University.

His current research interest includes stability and control of the grid-connected converter in photovoltaic power system.